Bulletin of the JSME Vol.7, No.5, 2020
Mechanical Engineering Journal

Determination of dynamic characteristics of piston-hole-type and bypass-pipe-type oil dampers using computational fluid dynamics

Itsuro HONDA*, Toshihiko ASAMI* and Hidetaka SHIOZAKI*
* Department of Mechanical Engineering, University of Hyogo
2167 Shosha, Himeji, Hyogo, 671-2280, Japan
E-mail: honda@eng.u-hyogo.ac.jp

Received: 4 April 2020; Revised: 27 May 2020; Accepted: 17 August 2020

Abstract
Oil dampers are indispensable devices for vibration suppression, but their nonlinear behavior makes it difficult to theoretically determine their damping characteristics. For that reason, the damping coefficient for oil dampers has conventionally been handled by introducing an experimentally determined constant into theoretical equations. In other words, the characterization of oil dampers has ultimately relied on experimentation. Fortunately, if the damping oil is a Newtonian fluid, the Navier–Stokes equations are able to accurately describe its movement. In our previous study, the Navier–Stokes equations were solved using the finite difference method and the damping coefficient was accurately calculated for an annular-channel-type oil damper. In this paper, we report the damping and added mass characteristics of the commonly used oil dampers, the piston-hole-type and bypass-pipe-type dampers, obtained using the finite difference method as in the previous report. The most basic design formula indicates that the damping coefficients for these dampers are the same when the flow paths are equal in length; however, it was demonstrated in this study that the damping characteristics of these dampers differ greatly depending on the shape of the convective vortex generated in the cylinder. The immersed boundary method was used in the present numerical analysis because the boundary of the fluid to be analyzed is surrounded by fixed and moving walls.

Keywords : Oil damper, Shock absorber, Piston-hole-type oil damper, Bypass-pipe-type oil damper, Computational fluid dynamics, Finite difference method, Immersed boundary method

1. Introduction

Oil dampers are indispensable devices for shock absorption and vibration suppression in many industrial applications, including shock absorbers for vehicles and seismic devices for building structures. However, because these devices are basically nonlinear, it is difficult to theoretically elucidate their damping performance, making it ultimately necessary to rely on experimentation. For example, the basic design formula for an oil damper with a narrow flow path includes an experimental constant, namely the flow coefficient, which is extremely difficult to calculate theoretically. Fortunately, if the damping oil is a Newtonian fluid, it is possible to clarify its nonlinear characteristics by solving the Navier–Stokes equations, and we have previously published a research paper to the annular-channel-type oil damper (Asami et al., 2014). In that study, it was demonstrated that the viscous damping force generated within the convective vortices present on either side of the piston can be estimated and that the estimated value exactly coincides with the experimental value.

In the present study, we applied this method to the widely used piston-hole-type (Asami et al., 1985) and bypass-pipe-type (Matsuoka et al., 2016) oil dampers, and compared their damping coefficient and the added mass effect from the oil flow. The added mass effect refers to the apparent increase in the mass of an object when it moves through a viscous fluid (Asami and Sekiguchi, 1988). In the most basic design formula, only the pressure loss along the flow path of these dampers is evaluated, so if the lengths of the flow paths of the two dampers are equal to each other, the dampers would be estimated to have exactly the same damping coefficient and added mass. However, it was demonstrate in this study that because the convective vortices generated on either side of the piston in these dampers have different shapes, the dampers show very different dynamic characteristics.

Paper No.20-00193
J-STAGE Advance Publication date : 24 August, 2020
[DOI: 10.1299/mej.20-00193]

Because the flow field to be analyzed in this study has both a fixed boundary and a moving boundary, the immersed boundary method (Roma et al., 1999) was adopted in the finite difference method. To more accurately calculate the flow in the cylinder, the flow field before and after the piston and the bypass pipe flow path should be individually divided into elements and connected using the overset grid method (Tahara et al., 2017); however, this requires the calculation of three-dimensional flows, which is a computationally demanding task. In this study, to reduce the calculation time, the flow in the cylinder was calculated as a two-dimensional flow by modifying the flow path shape.

2. Basic shape of oil dampers and conventional design formulae

Basically, oil dampers can be classified into three types, as shown in Fig. 1, according to their flow path shapes. In this figure, the piston rod is omitted for simplicity. In the piston-hole-type and bypass-pipe-type dampers shown in Fig. 1(b) and (c), respectively, it is assumed that (1) both fluids flow only in the circular hole flow path with inner diameter d_o, (2) the piston diameter d_p is equal to the cylinder inner diameter d_c, and (3) no friction occurs between the two walls. In the most basic design formula for an oil damper, the pressure drag caused by the pressure loss of the fluid inside the flow path is treated as a force proportional to the piston velocity, and that caused by the convective vortices generated on either side of the piston is treated as proportional to the square of the piston velocity. Thus, the damping coefficient c for these oil dampers is given by (Nakane, 1966)

$$c = \alpha A_p^2 + \frac{\rho A_p^3}{2c_d^2 A_o} \upsilon_p. \tag{1}$$

For the annular-channel-type oil damper shown in Fig. 1(a), the flow resistance coefficient α used here is given by

$$\alpha = \frac{12\mu l}{\pi d_p h^3}. \tag{2}$$

For the piston-hole-type and bypass-pipe-type oil dampers shown in Fig. 1(b) and (c)

$$\alpha = \frac{8\pi\mu l}{(\pi d_o/2)^4}. \tag{3}$$

Here, μ and ρ represent the viscosity coefficient and the density of the fluid, respectively. In addition, l is the flow path length, which corresponds to the piston length l_p in the dampers shown in Fig. 1(a) and (b) and the bypass pipe length $l_1 + 2l_2$ in the damper shown in Fig. 1(c). Furthermore, A_p ($= \pi d_p^2/4$) and A_o ($= \pi d_o^2/4$) are the cross-sectional areas of the piston and the flow path, respectively; h ($= (d_c - d_p)/2$) is the radius clearance; and υ_p is the piston velocity. Finally, c_d represents the flow coefficient, which depends on the shape of the opening and is determined experimentally. The viscous drag expressed in Eqs. (2) and (3) takes into account only the pressure loss along the flow path, and the pressure loss in the convective vortices present on either side of the piston (this is also a viscous drag) is not evaluated at all in these design formulae. Therefore, the same design formula is used to represent the dampers shown in Fig. 1(b) and (c) despite these dampers having flow paths with completely different shapes.

3. Analytical model for oil damper and governing equations

The governing equation of the oil damper used in this study is expressed in vector form as

$$\left.\begin{aligned} &\frac{\partial \mathbf{V}}{\partial t} + (\mathbf{V}\cdot\nabla)\mathbf{V} = -\nabla p + \frac{1}{Re}\nabla^2\mathbf{V} \\ &\nabla\cdot\mathbf{V} = 0. \end{aligned}\right\} \tag{4}$$

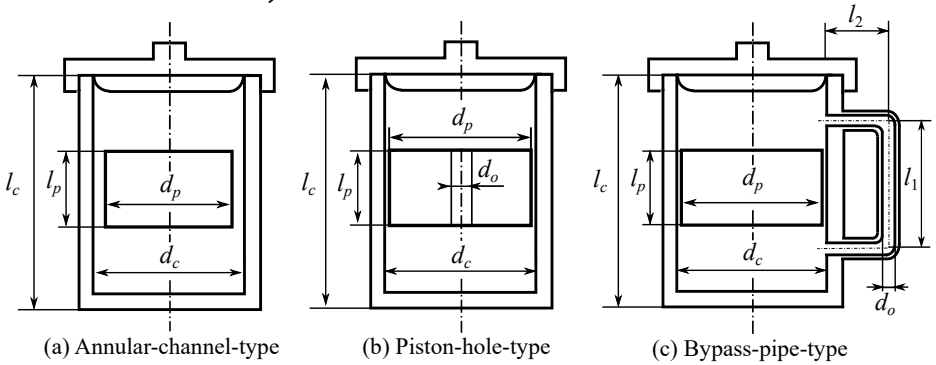

(a) Annular-channel-type (b) Piston-hole-type (c) Bypass-pipe-type

Fig. 1 Three typical types of oil dampers

[DOI: 10.1299/mej.20-00193]

The first formula in Eq. (4) is the Navier–Stokes equation for an incompressible fluid expressed in the Cartesian coordinate system. The first term on the left-hand side of this equation is the unsteady term, and the second term is the convective term. On the right-hand side, the first term is called the pressure term, and the second term is the viscous term. Equation (2) is the solution obtained by setting all the terms on the left-hand side to zero in the first formula in Eq. (4). The second formula in Eq. (4) is a continuous equation for an incompressible fluid. Furthermore, the Reynolds number $Re = VL/\nu$ in Eq. (4) is defined by a characteristic length L, the flow speed V, and the kinematic viscosity ν of the fluid. Here, the characteristic length is the inner radius $d_c/2$ of the cylinder, and the flow speed is set equal to the maximum piston velocity v_p. All parameters used in Eq. (4) are also non-dimensionalized with respect to the characteristic length and flow speed.

In solving Eq. (4) numerically, to reduce the calculation time, the shapes of the flow paths of the oil dampers shown in Fig. 1(b) and (c) were changed as shown in Fig. 2(a) and (b), respectively. The flow in the cylinder and along the flow path was analyzed as a two-dimensional flow in the xz plane in this figure. It should be noted that the length scales in the x- and y-directions in Fig. 2 are not the same.

4. Numerical methods

4.1. Difference approximation of convective term

Inside the oil damper, vortices of various sizes repeatedly form and disappear, creating a complicated flow. In the Navier–Stokes equation, this complicated vortex formation is expressed by the second term (convective term) on the left-hand side of the first formula in Eq. (4). Because this term is nonlinear, it greatly affects the accuracy and stability of the equation when it is discretized. To demonstrate the stability of the calculation, a single component of the second term on the left-hand side of Eq. (4), $u\,\partial u/\partial x$, is considered. Here, $u(x,t)$ is the velocity along the x axis, and it is assumed that it has the following periodic behavior:

$$u = f \sin kx, \tag{5}$$

where k is the wave number and f is a constant. In this case, the expression $u\,\partial u/\partial x$ is expressed as

$$u\frac{\partial u}{\partial x} = kf^2 \sin kx \cos kx = \frac{1}{2}kf^2 \sin 2kx. \tag{6}$$

As this equation shows, when a certain fluctuation occurs in the fluid, a frequency component greater than the fluctuation frequency is generated. Normally, this frequency component is attenuated quickly by the viscous action of the fluid. However, in the finite difference method, because the motion of the fluid is treated discretely, the high-frequency components are not attenuated unless the computational grid is made to be very fine, and the calculation becomes unstable. Numerical viscosity is introduced into the finite difference equation to prevent this destabilization. Upwind difference (Leonard, 1979), which is one of the schemes equipped with a numerical filter to remove such high-frequency components, is a difference method that involves placing a weight on the upstream side in consideration of the flow originating upstream. In this study, we used the Kawamura-Kuwahara scheme (Kawamura and Kuwahara, 1984), which is an extension of the third-order upwind difference equation:

$$f\left.\frac{\partial u}{\partial x}\right|_{x=x_i} = f\,\frac{-u_{i+2} + 8(u_{i+1} - u_{i-1}) + u_{i-2}}{12\Delta x} + \alpha\frac{|f|}{12}\,\frac{u_{i+2} - 4u_{i+1} + 6u_i - 4u_{i-1} + u_{i-2}}{\Delta x^4}. \tag{7}$$

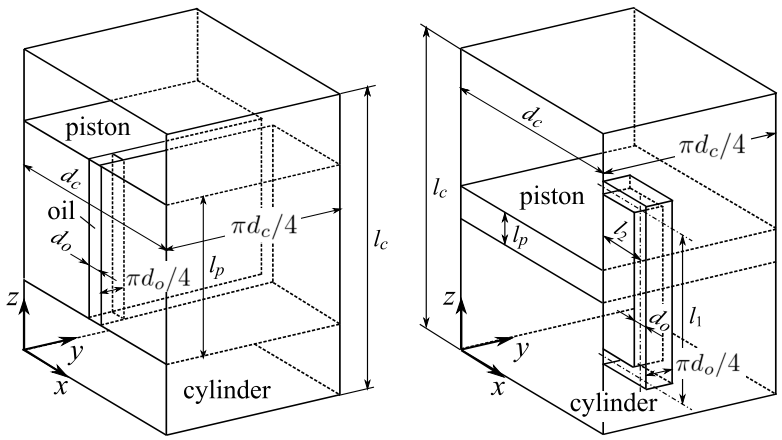

(a) Piston-hole-type oil damper (b) Bypass-pipe-type oil damper

Fig. 2 Analytical model of oil dampers for numerical calculation

[DOI: 10.1299/mej.20-00193]

The first term on the right-hand side of this equation is the central difference equation with fourth order accuracy, and the second term is a numerical viscosity term with an approximation of the fourth derivative. Additionally, α is a weighting factor that determines the magnitude of the numerical viscosity, and here $\alpha = 3.0$ was used.

4.2. Time marching method

The properties of a differential equation are determined by its highest-order derivative. The Navier–Stokes equation has the characteristics of a diffusion equation because this is the second derivative. Therefore, when the explicit scheme is applied to time marching, there are severe restrictions on the time step size. To avoid these restrictions, the implicit scheme is typically used for the time marching of this equation. However, because the convective term is nonlinear, treating this part in an implicit scheme not only makes it difficult to solve the equation numerically but also means that high-precision calculations cannot be performed because a phase error is likely to occur in periodic motion. Therefore, to handle the convective term in an explicit scheme, the following temporal linearization was performed:

$$(\mathbf{V}^{n+1} \cdot \nabla)\mathbf{V}^{n+1} \simeq (\mathbf{V}^{n} \cdot \nabla)\mathbf{V}^{n+1}, \tag{8}$$

where the superscript indicates the number of time steps. In contrast, the viscosity term is treated implicitly so that the time step can be made large.

Using this concept, an intermediate velocity $\tilde{\mathbf{V}}$ was introduced to the time marching, the second-order Adams–Bashforce method (Butcher, 2003) was applied to the convective term, and the second-order Crank–Nicolson method was applied to the viscous term. Temporal discretization was then performed by the following fractional-step method (Kim and Moin, 1985):

$$\frac{\tilde{\mathbf{V}} - \mathbf{V}^{n}}{\Delta t} + \frac{1}{2}\left(3\mathbf{H}^{n} - \mathbf{H}^{n-1}\right) = \frac{1}{2Re}\left(\nabla^2\tilde{\mathbf{V}} + \nabla^2\mathbf{V}^{n}\right) \tag{9}$$

and

$$\frac{\mathbf{V}^{n+1} - \tilde{\mathbf{V}}}{\Delta t} = -\nabla p^{n+1}, \tag{10}$$

where $\mathbf{H}$ represents the convective term and is defined by

$$\mathbf{H} = -(\mathbf{V} \cdot \nabla)\mathbf{V}. \tag{11}$$

The intermediate velocity $\tilde{\mathbf{V}}$ calculated from Eq. (9) is the velocity calculated by removing the pressure term from the Navier–Stokes equation. That is, Eq. (9) does not consider the effect of pressure. For the time marching of the pressure, the following Poisson equation was used:

$$\nabla^2 p^{n+1} = \frac{\nabla \cdot \tilde{\mathbf{V}}}{\Delta t}. \tag{12}$$

This equation is derived by taking the divergence of Eq. (10) and setting $\nabla \cdot \mathbf{V}^{n+1} = 0$, which is obtained because the continuous equation holds for the $n+1$ time step, i.e., for the next time step. In this way, time marching with second order accuracy can be performed in three steps in the order of Eqs. (9), (12), and (10).

4.3. Immersed boundary method

In our previous paper (Asami, 2014), the grid division method applied to fluid flow was the arbitrary Lagrangian–Eulerian (ALE) method (Hirt et al., 1974). This method uses a calculation grid in the cylinder with the moving piston surface or the inner surface of the fixed cylinder as the boundary surface. Because the piston considered in our previous study moves unsteadily, the coordinates of the calculation grid in the cylinder change constantly. When this method is applied to a bypass-pipe-type oil damper, which is the subject of this study, this causes the problem of the relative values of grid point coordinates in the cylinder and those in the bypass channel always changing with time. To solve this problem, a solution called the overset grid method (Tahara et al., 2017) may be applied. However, this method not only complicates the calculation procedure but also reduces the accuracy of mass and momentum storage. Therefore, we performed discretization using the equally spaced difference method and applied the immersed boundary method (Roma et al., 1999) to reproduce the moving piston.

This method will be described with reference to the case where the moving piston wall is between grid lines j and $j+1$ as shown in Fig. 3. The Navier–Stokes equations have first and second order differential terms describing physical quantities such as flow velocity and pressure, and these are discretized using the finite difference method. Here, for the

[DOI: 10.1299/mej.20-00193]

sake of simplicity, it is assumed that the convective term is also discretized with second-order accuracy. In ordinary discretization using the central difference of second-order accuracy, the physical quantity to be discretized is represented as ϕ as follows:

$$\frac{\partial \phi}{\partial x} = \frac{\phi_{j+1} - \phi_{j-1}}{2\Delta x}, \quad \frac{\partial^2 \phi}{\partial x^2} = \frac{\phi_{j+1} - 2\phi_j + \phi_{j-1}}{\Delta x^2}. \tag{13}$$

At this time, if the piston wall position is between grid lines j and $j+1$ as shown in Fig. 3, discretization using the above equation will not evaluate the piston velocity at the correct position. In addition, it is possible that there will be a mass flux error, disobeying the law of conservation of mass and conservation of momentum. Therefore, the physical quantity between grid lines j and $j+1$ is given by the following linear interpolation:

$$\phi_j = \frac{\varepsilon}{\varepsilon + 1}\phi_{j-1} + \frac{1}{\varepsilon + 1}\phi_{\text{piston}}. \tag{14}$$

By setting the calculation boundary on grid line j using this value as the boundary value, it is possible to perform the calculation with the effect of the piston velocity taken into consideration while using the conventional difference approximation formula.

The pressure is calculated by solving the above-mentioned Poisson equation and applying the Neumann-type boundary condition with a specified gradient and must therefore be handled differently from the velocity. Normally, the pressure gradient on the body surface is assumed to be zero, so the second derivative of the pressure at the piston surface is zero. At this time, the second derivative of pressure can be linearly interpolated as follows:

$$\left(\frac{\partial^2 p}{\partial x^2}\right)_j = \frac{\varepsilon}{\varepsilon + 1}\left(\frac{\partial^2 p}{\partial x^2}\right)_{j-1} + \frac{1}{\varepsilon + 1}\left(\frac{\partial^2 p}{\partial x^2}\right)_{\text{piston}} = \frac{\varepsilon}{\varepsilon + 1}\left(\frac{\partial^2 p}{\partial x^2}\right)_{j-1}. \tag{15}$$

In this way, the pressure is numerically calculated by setting grid line j including the effect of the piston as the calculation boundary, in the same manner as with the velocity.

5. Verification of the accuracy of the immersed boundary method

To verify the accuracy of the immersed boundary method described in Section 4.3, we calculate a Hagen–Poiseuille flow whose exact solution is known. When the radial coordinate of the pipe is r and the axial coordinate is z, the exact solution of the velocity and pressure gradient is given by

$$v(r) = 2v_{\text{ave}}\left[1 - \left(\frac{r}{R}\right)^2\right], \quad \frac{\partial p}{\partial z} = -\frac{8}{R^2}\frac{v_{\text{ave}}}{Re}, \tag{16}$$

where R is the inner radius of the pipe and v_{ave} is the average flow velocity inside the pipe.

A Hagen–Poiseuille flow is a steady laminar solution of an incompressible Newtonian fluid flowing in a circular pipe with a constant diameter. To realize this flow with the unsteady Navier–Stokes equation, a piston is placed at the left end ($z = 0$) of the circular pipe and made to move at a constant acceleration of $a = 0.1$ from $t = 0$ to $t = 10$, where t is the dimensionless time. Next, from $t = 10$ to $t = 20$, the piston is given a constant velocity of $v_p = 1.0$. With a time step of $\Delta t = 0.001$ and $n = 20000$ repetitions, the velocity and pressure gradients are calculated by the immersed boundary method up to $t = 20$. Figure 4 shows the results at $t = 20$ with the numerical solutions represented as white circles and the exact solutions calculated from Eq. (16) shown as solid lines. Figure 4(a) shows the axial velocity distribution at the pipe outlet, and Fig. 4(b) shows the pressure distribution from the piston wall ($z = 15$) to the pipe outlet ($z = 20$). The white circles in these figures indicate the numerical solutions for all grid points. From these figures, it was confirmed that the numerical and exact solutions are in good agreement. However, the numerical solution is taken after the transition from unsteady to steady motion, and the pressure gradient shown in Fig. 4(b) still retains the effect of unsteady motion. In the numerical solution shown in Fig. 4(a), the reason that $v = 2$ was not achieved at $r = 0$ is that the initial inflow velocity assumed to be a uniform flow of $v = 1$ was not completely satisfied because the fluid velocity becomes zero at the wall grid points. As a result, the numerical solution inevitably has a lower total flow rate than the analytical solution.

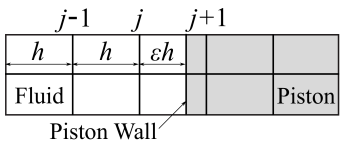

Fig. 3 Diagram of grid division including the moving piston wall

[DOI: 10.1299/mej.20-00193]

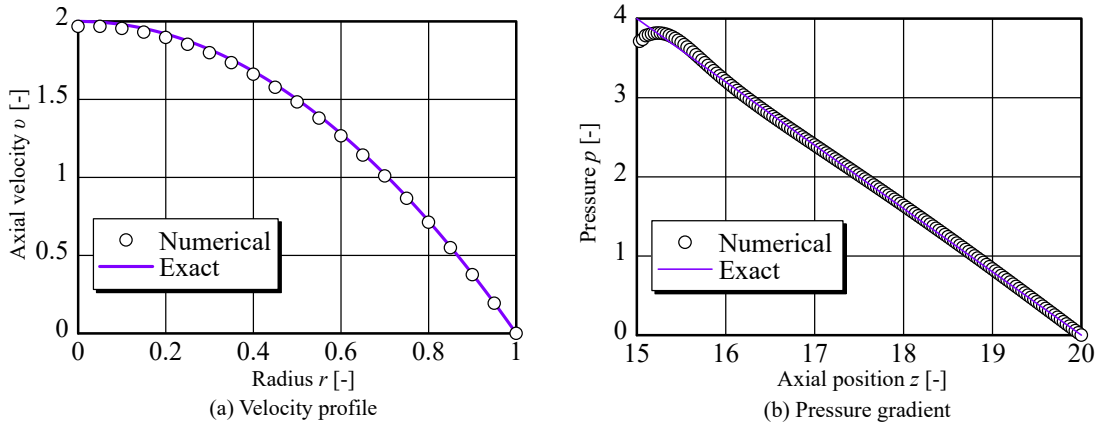

(a) Velocity profile (b) Pressure gradient

Fig. 4 Exact and numerical solutions in a Hagen–Poiseuille flow

Table 1 Dimensions of the damper in Fig.1(b)

d_c	40 mm
d_p	40 mm
d_o	4 mm
l_c	80 mm
l_p	40 mm
n_x	200
n_z	400
n_t	200
ν	100 mm^2/s
ρ	968 kg/m^3

Table 2 Dimensions of the damper in Fig.1(c)

d_c	40 mm
d_p	40 mm
d_o	4 mm
l_c	80 mm
l_p	6 mm
n_x	200
n_z	400
n_t	200
l_1	30 mm
l_2	5 mm

6. Numerical analysis results

Tables 1 and 2 give the specifications of the oil dampers shown in Fig. 1(b) and (c), respectively. Both dampers have a channel length of 40 mm. Symbols n_x and n_z in the tables are the number of divisions of cylinder diameter d_c and cylinder length l_c, respectively. In addition, n_t is the number of divisions per period of the piston undergoing sinusoidal oscillation. Damping oil with the same physical properties is used for both oil dampers, and the kinematic viscosity ν and density ρ of the oil are given in Table 1.

All figures shown below are numerical solutions under steady-state vibration conditions. Steady-state was judged by whether the difference was less than 1% compared to the value one cycle ago.

6.1. Diagrams of velocity profile and pressure distribution in cylinder

Figures 5 and 6 show instantaneous velocity profiles and pressure distributions in the piston-hole-type oil damper shown in Fig. 2(a) when the piston is sinusoidally oscillating with amplitude $a = 2.1$ mm and frequency $f = 30$ Hz. Figure 5 shows the moment when the piston has moved by a distance of $x = a/2$ from its vibration center toward the top dead center. At this time, the piston is moving upward while decelerating, and the fluid is flowing down the flow path from top to bottom. Behind the piston, twin vortices have been formed by the jet from the piston hole. The twin vortices seen in front of the piston are remnants of the vortices formed by the piston movement half a cycle previously. Naturally, the pressure is low at the center of the vortex, and the pressure in front of the piston is higher than that behind the piston.

Figure 6 shows the velocity profile and pressure distribution at the moment when the piston reaches its top dead center. Because of the influence of the inertial force of the fluid, the phase of the pressure is always advanced with respect to the displacement of the fluid movement. The pressure behind the piston is already higher than the forward pressure. In addition, the pressure drop at the center of the vortex is more clearly observable because the overall pressure behind the piston has increased.

Similarly, Figs. 7 and 8 show the velocity profiles and pressure distributions in the bypass-pipe-type oil damper shown in Fig. 2(b), and the calculation conditions and the instants in the piston movement cycle are the same as in Figs. 5 and 6, respectively. Because the jet outlet is on the cylinder side wall, it can be clearly seen that the vortex generation situation is completely different from that for the piston-hole-type oil damper. In particular, three vortices with different sizes formed behind the piston, indicating that the vortices change their shape over time.

[DOI: 10.1299/mej.20-00193]

6.2. Relationship between piston input displacement and output drag force

Figure 9(a) shows the relationship between the displacement x applied to the piston of an oil damper and the force F_T transmitted to the foundation via the spring and dashpot of the Voigt-type vibratory system. The mass of this system is supported on a fixed foundation by a massless linear spring with a spring constant k and a massless dashpot with a damping coefficient c, and is subjected to a sinusoidal displacement $x(t) = a \sin \omega t$.

If the damping ratio of the system, $\zeta = c/(2\sqrt{mk})$, is zero, the relationship between x and F_T is described by a straight line rising to the right. However, if the damping ratio ζ is nonzero, the input–output relationship follows an elliptical hysteresis curve. (In the case shown in Fig. 9(a), the excitation frequency ω is the same as the undamped natural angular frequency $\omega_n = \sqrt{k/m}$ of the system.) If the spring is removed from this vibration system, the inclination of the ellipse becomes zero; if this dashpot is then also replaced by a damper with an added mass of m_A, the relationship between the drag force $D(t)$ acting on the piston and the displacement of the piston becomes an ellipse descending to the right, as shown in Fig. 9(b). (In this figure, the value of $m_A a\omega^2$ is set to 1.)

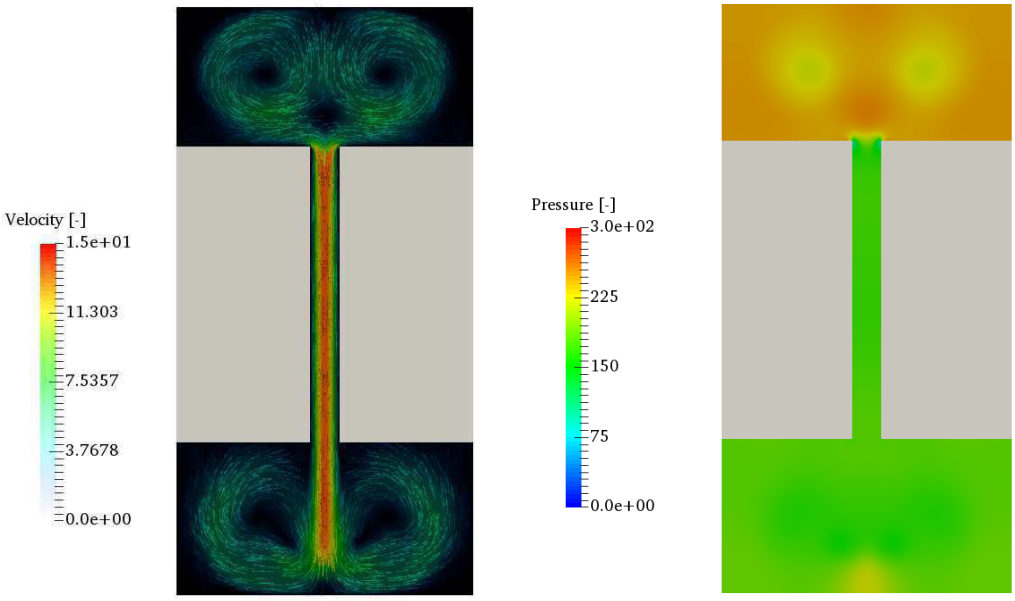

(a) Velocity profile (b) Pressure distribution

Fig. 5 Velocity and pressure for the piston-hole-type oil damper at a deceleration stage ($f = 30$ Hz, $a = 2.1$ mm, $x = a/2$)

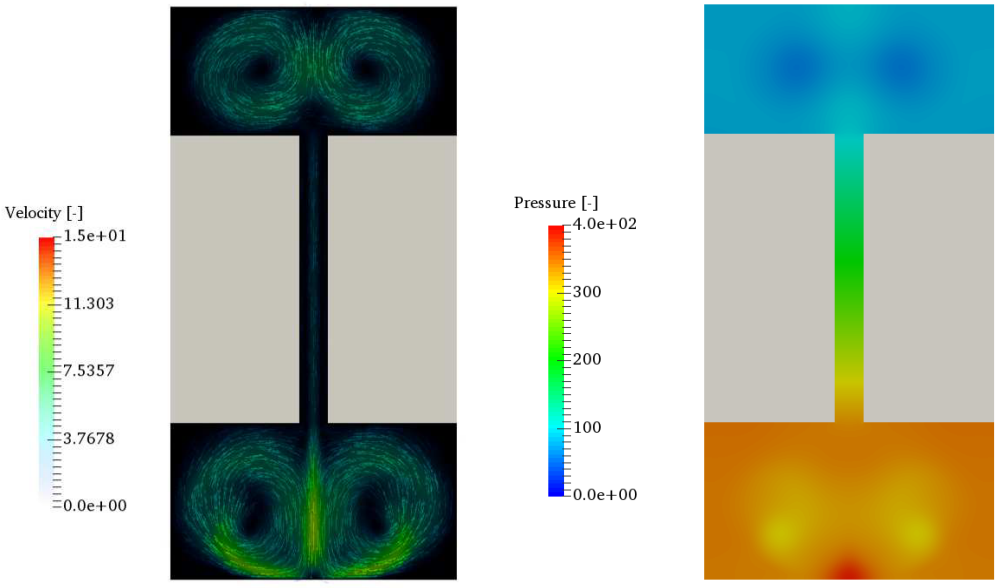

(a) Velocity profile (b) Pressure distribution

Fig. 6 Velocity and pressure for the piston-hole-type oil damper at the top dead center ($f = 30$ Hz, $a = 2.1$ mm, $x = a$)

[DOI: 10.1299/mej.20-00193]

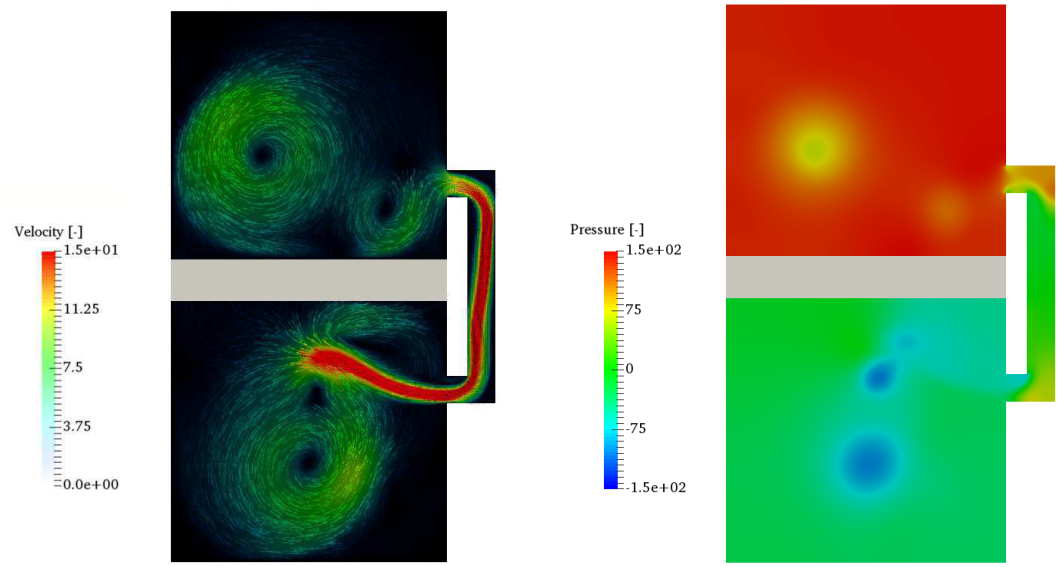

(a) Velocity profile (b) Pressure distribution

Fig. 7 Velocity and pressure for the bypass-pipe-type oil damper at a deceleration stage (f = 30 Hz, a = 2.1 mm, $x = a/2$)

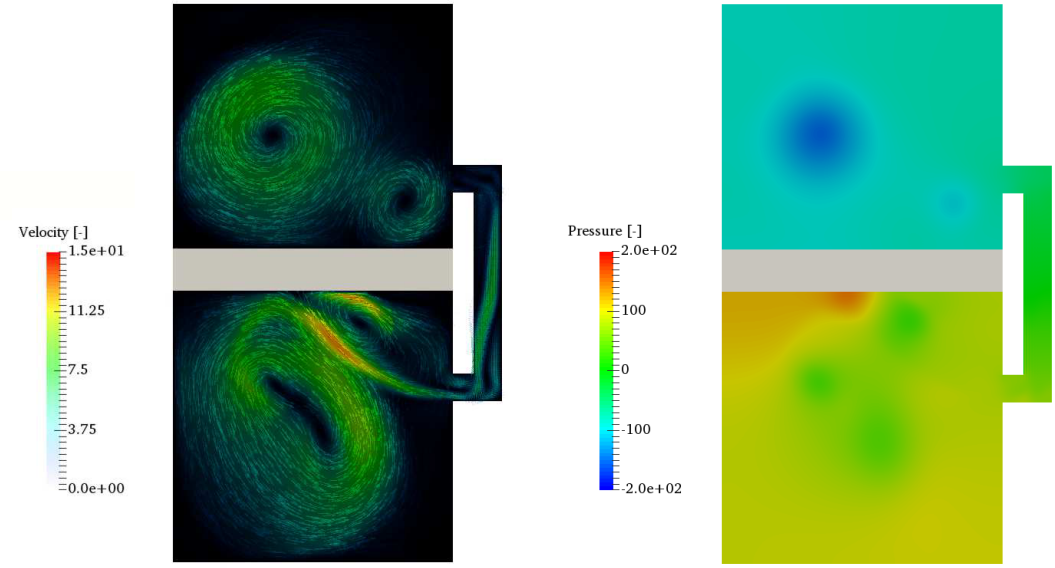

(a) Velocity profile (b) Pressure distribution

Fig. 8 Velocity and pressure for the bypass-pipe-type oil damper at the top dead center (f = 30 Hz, a = 2.1 mm, $x = a$)

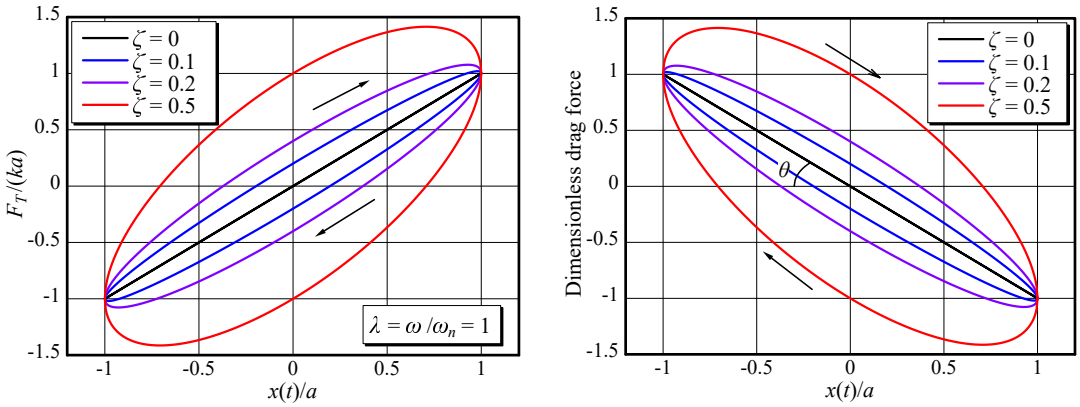

(a) Voigt-type vibration system (b) Relationship piston motion and fluid force acts on the piston

Fig. 9 Load-displacement curves for a SDOF system and an oil damper subjected to a harmonic motion

[DOI: 10.1299/mej.20-00193]

Figures 10 and 11 show the relationship between the piston displacement and the drag force at piston frequencies of 5 and 30 Hz, respectively. Figures 10(a) and 11(a) show cases where the piston amplitude is 0.3 mm, and Figs. 10(b) and 11(b) show cases where the piston amplitude is 2.1 mm. The piston drag is calculated by integrating the pressure on the front and back of the piston over the entire surface in the pressure distribution diagrams shown in Figs. 5–8. As is evident from Figs. 10 and 11, the calculated hysteresis curves are almost elliptical and descend to the right. By measuring the gradient θ (see Fig. 9(b)) of this ellipse, the apparent mass increase of the piston (i.e., the added mass m_A) can be obtained. Furthermore, the damping coefficient c for the oil damper can be estimated from the area of the ellipse.

When the piston moves with a low frequency and small amplitude, the distortion of the ellipse is small, but as these increase, the distortion increases, as shown in Fig. 11(b). Furthermore, there is a big difference between the elliptical shapes for the piston-hole-type and bypass-pipe-type oil dampers, especially at high frequencies.

6.3. Damping coefficient and added mass of oil dampers

Figure 12(a) and (b) shows the amplitude dependency of the damping coefficient for each oil damper at piston frequencies of 5 and 30 Hz, respectively. As shown in the figure, the damping coefficient for the bypass-pipe-type oil damper shows a clear linear dependence on the piston amplitude. In contrast, the damping coefficient for the piston-hole-type oil damper does not show a significant amplitude dependency. The characteristic feature of the piston-hole-type oil damper is that its damping coefficient has a minimum value at a certain vibration amplitude. The damping coefficient for both oil dampers increases as the piston frequency increases, and this is especially true for the bypass-pipe-type oil damper.

Similarly, Fig. 13(a) and (b) shows the added mass effect plotted against the piston amplitude at piston frequencies of 5 and 30 Hz, respectively. It is considered that the added mass increases as the fluid is stirred more rigorously in the cylinder. The added mass for the piston-hole-type oil damper is a larger than that for the bypass-pipe-type damper, so it is considered that the former has a faster vortex flow. When the frequency of the piston is low, the added mass increases with increasing vibration amplitude. However, at high frequency, the added mass first decreases and then increases for the piston-hole-type damper, whereas for the bypass-pipe-type damper, it first increases and then decreases.

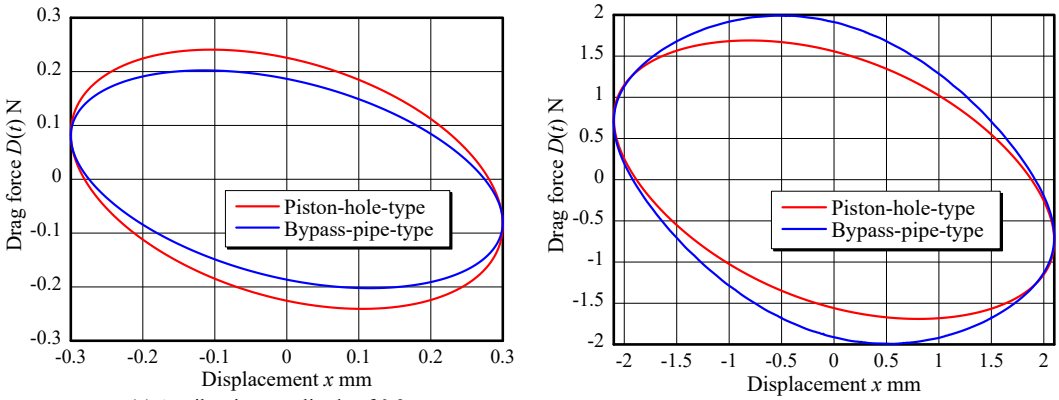

(a) At vibration amplitude of 0.3 mm (b) At vibration amplitude of 2.1 mm

Fig. 10 Drag force acting on a piston moving at a frequency of 5 Hz

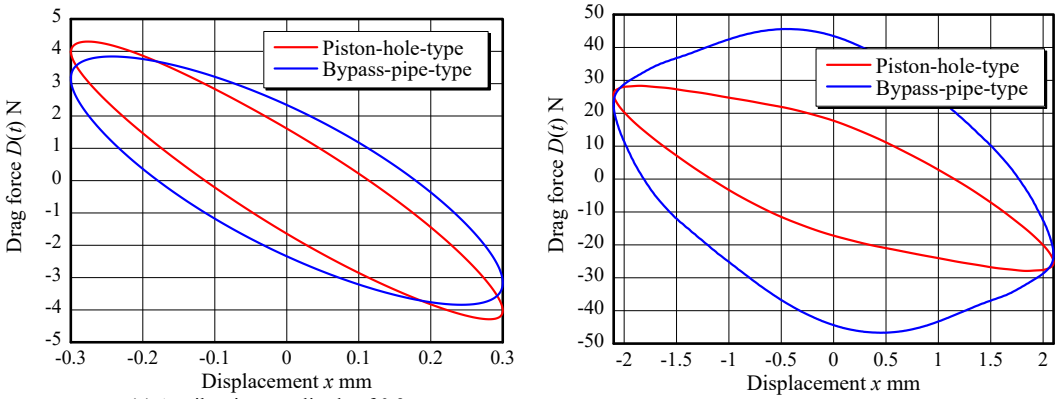

(a) At vibration amplitude of 0.3 mm (b) At vibration amplitude of 2.1 mm

Fig. 11 Drag force acting on a piston moving at a frequency of 30 Hz

[DOI: 10.1299/mej.20-00193]

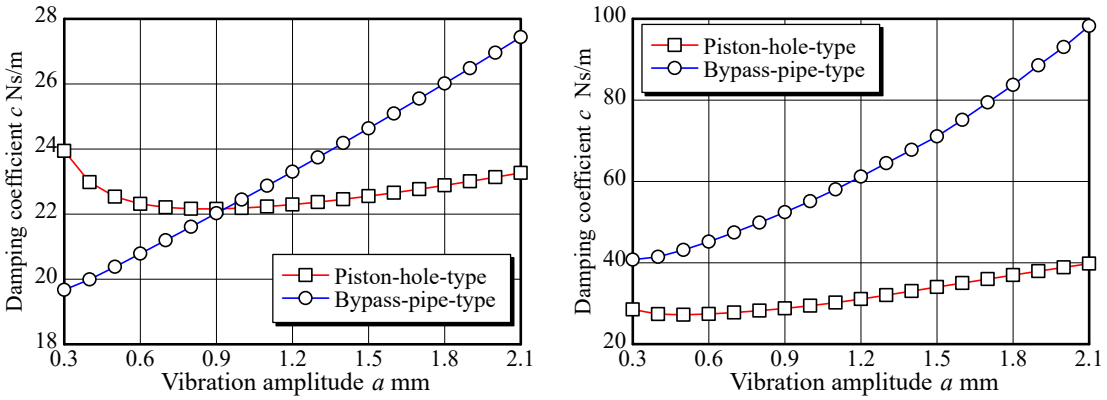

Fig. 12 Damping coefficient for the oil dampers for various vibration amplitudes

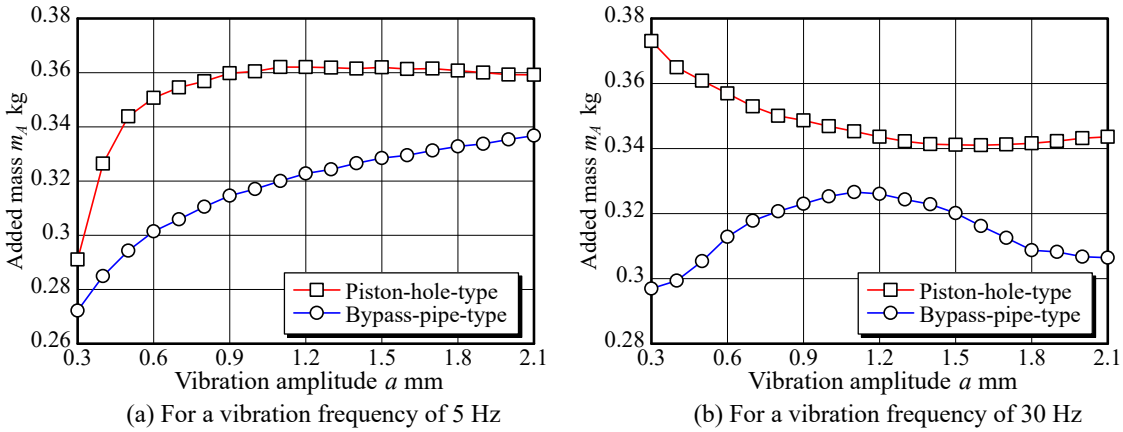

Fig. 13 Added mass for the oil dampers for various vibration amplitudes

7. Conclusion

The conventional design formulae (Eqs. (2) and (3)) for viscous oil dampers were obtained by approximately calculating the pressure drop in the flow path, without taking into account the effects of convective vortices generated around the piston. In contrast, the design formula (second term of Eq. (1)) for a dynamic oil damper is an empirical formula and ultimately must rely on data collection from many experiments. The aim of this study was to accurately estimate the pressure drop occurring in complex convective vortices generated in the cylinder by numerically solving the Navier–Stokes equation. With this approach, it was possible to calculate the difference between the damping coefficient and the added mass for piston-hole-type and bypass-pipe-type oil dampers. The results obtained in this study can be summarized as follows:

(1) It was demonstrated that numerical calculations can be performed efficiently by applying the immersed boundary method to the finite difference method, even when the target has both a moving boundary and a fixed boundary in a cylinder, as in the case of a bypass-pipe-type oil damper.

(2) It was possible to clarify the difference between the dynamic characteristics of the piston-hole-type and bypass-pipe-type oil dampers, which was not precisely known prior to this study.

(3) In the piston-hole-type oil damper, twin vortices were observed to appear symmetrically behind the piston, and the distortion of the elliptical hysteresis curve that describes the load–displacement relationship was small. In the bypass-pipe-type oil damper, it was confirmed that complicated vortices were generated, and the ellipse was greatly distorted.

(4) The amplitude dependency of the damping coefficient of the oil damper is larger for the bypass-pipe-type damper than for the piston-hole-type damper, and increases almost linearly with increasing vibration amplitude.

(5) The added mass is larger for the piston-hole-type oil damper than for the bypass-pipe-type damper, and increases with increasing the vibration amplitude at low frequencies, but exhibit a more complex response at high frequencies.

(6) Until now, experimental verification of the performance of oil dampers has been required, but the numerical simulations carried out in the present study have shown that a detailed design can be performed using this approach.

[DOI: 10.1299/mej.20-00193]

References

Asami, T., Sekiguchi, H., and Taniguchi, S., "Study on the Oil Damper with Variable Damping Mechanism (1st Report, Damping Characteristics of the Damper with a Piston Having Cylindrical Orifices," Bulletin of the JSME, Vol.28, No.246 (1985), pp.2978-2985.

Asami, T., and Sekiguchi, H., "Study on an Oil Damper with a Variable Damping Mechanism (Damping Characteristics of a Damper with a Piston Having a Fan-Shaped Orifice," JSME International Journal Ser. Ⅲ, Vol.31, No.2 (1988), pp.370-379.

Asami, T., Honda, I., and Ueyama, A., "Numerical Analysis of the Internal Flow in an Annular Flow Channel Type Oil Damper," ASME Journal of Fluids Engineering, Vol.136, No.3 (2014), p.031101.

Butcher, John C., Numerical Methods for Ordinary Differential Equations, John Wiley (2003), p.103.

Hirt, C. W., Amsden, A. A., and Cook, J. L., "An Arbitrary Lagrangian-Eulerian Computing Method for All Flow Speeds," Journal of Computational Physics, Vol.14 (1974), pp.227-253.

Kawamura, T., and Kuwahara, K., "Computation of High Reynolds Number Flow Around a Circular Cylinder with Surface Roughness," AIAA Paper 84-0340 (1984).

Kim, T., and Moin, P., "Application of a Fractional-Step Method to Incompressible Navier-Stokes Equations," Journal of Computational Physics, Vol.59 (1985), pp.308-323.

Leonard, B. P., "A Stable and Accurate Convective Modelling Procedure Based on Quadratice Upstream Interpolation," Comput. Meths. Appl. Mech. Eng., Vol.19 (1979), pp.59-98.

Matsuoka, T., Hiramoto, K., Sunakoda, K., Abe, N., and Lin, P., "Fluid Inertia Damper Using MR Fluid with a Long Spiral Bypass Pipe," Mechanical Engineering Journal, Vol.3, No.2 (2016), DOI:10.1299/mej.15-00731.

Nakane, Y., Springs, Absorbers and Brakes, Seibundo-Shinkosha (1966), pp.187-196 (in Japanese).

Roma, A. M., Peskin, C. S., and Berger, M. J., "An Adaptive Version of the Immersed Boundary Method," Journal of Computational Physics, Vol.153, No.2 (1999), pp.509-534.

Tahara, Y., Shingo, S., Kanai, A., "CFD Based Optimal Design Method for Energy Saving Devices by Using Overset Grid Technique and Nonlinear Optimization Theory," Journal of the Japan Society of Marine and Marine Engineering, Vol.26 (2017), pp.1-16 (in Japanese).

[DOI: 10.1299/mej.20-00193]